An Accelerated Recurrent Neural Network for Visual Servo Control of a Robotic Flexible Endoscope with Joint Limit Constraint

Weibing Li, Chengzhi Song, and Zheng Li, *Member, IEEE*

***Abstract*—A recurrent neural network (RNN) is accelerated and applied to visual servo control of a physically-constrained robotic flexible endoscope. The robotic endoscope consists of a patient side manipulator (PSM) of the da Vinci Research Kit (dVRK) platform and a flexible endoscope working as an end-effector. To automate the robotic endoscope, kinematic modeling for visual servoing is conducted, leading to a quadratic programming (QP) control framework incorporating kinematic and physical constraints of the robotic endoscope. To solve the QP problem and realize the vision-based control, an RNN accelerated to finite-time convergence by a sign-bi-power activation function (SBPAF) is proposed. The finite-time convergence of the RNN is theoretically proved in the sense of Lyapunov, showing that the SBPAF activated RNN exhibits a faster convergence speed as compared with its predecessor. To validate the efficacy of the RNN model and the control framework, simulations are performed using a simulated flexible endoscope in the robot operating system (ROS). Physical experiment is then further performed to verify the feasibility of the RNN model and the control framework. Both simulation and experimental results demonstrate that the proposed RNN solution is effective to achieve visual servoing and handle physical limits of the robotic endoscope simultaneously.**

***Index Terms*—Finite-time convergence, flexible endoscope, recurrent neural network, visual servo control.**

I. Introduction

In minimally invasive surgery, the endoscope plays a significant role in visualizing the operative site inside a patient's body [1], [2]. Operating the endoscope appropriately and timely is crucial to secure the safety and efficiency of a surgery. Conventionally, a human assistant is required to manually adjust the endoscope during the surgical operations. The endoscope assistant unavoidably suffers from hand tremors, which leads to unstable camera views. The assistant may misunderstand the surgeon's intentions and then operate the endoscope inappropriately, which lowers the efficiency of the surgery. To overcome the limitations incurred by a human assistant, robotic endoscope holders such as the AESOP, EndoAsist, ViKY and endoscopic camera manipulator of the da Vinci surgical system have been developed [1], [2]. The endoscope assistant can be replaced with a robotic endoscope, allowing the surgeon to operate the robotic endoscope directly. This alleviates hand tremors and inefficient communications between the surgeon and the human assistant.

An endoscope camera is usually jointed with a rigid shaft. The motions of the rigid shaft inserted into the surgical site through a trocar must respect the constraints of the trocar [2], [3]. As compared with a typical six-joint industrial robot, a rigid endoscope robot suffers from a loss of two translation degrees-of-freedom (DOFs). To obtain improved flexibility and dexterity, flexible endoscopes have been physically implemented [4]–[11]. For instance, a semi-automatic flexible endoscope driven by two cables was designed in [6], where the endoscope equipped with sensors has capabilities to achieve collision avoidance. The flexible continuum robot designed in [7] has potentials to improve a spring backbone endoscope presented in [8] due to the enhanced flexibility by its redundancy. Flexible endoscopes were experimentally demonstrated to offer enhanced safety [5] and wider vision scope [9] as compared with rigid endoscopes. Hence, it is meaningful to investigate flexible endoscopes for surgical applications.

Traditionally, interactions between the surgeon and the robotic endoscope are achieved by manual manipulation or teleoperation. Although these robotic endoscopes allow a surgeon to perform a solo surgery, the operation of the endoscope imposes extra burdens on the surgeon. To further relieve the surgeon's workload, automation technologies have been introduced to robotic endoscopes. A common way to automate a robotic endoscope is to form a control system using the visual information retrieved from the endoscope camera, considering that vision is a naturally integrated sensor of an endoscope [2]–[5]. For example, a flexible endoscope was robotized to automatically track an anatomical target of interest in [4], freeing the surgeon of the task for stabilizing the anatomical target on the image plane. In [5], the patient side manipulator (PSM) of the da Vinci Research Kit (dVRK) platform equipped with a flexible endoscope was endowed with autonomy by using visual servo control.

One common drawback of the visual servo control frameworks presented in [3]–[5] is that joint limits such as the

This work was supported by the Hong Kong RGC General Research Fund with Project No. 14207017, 14203019, the Early Career Scheme 24204818, the Innovative Technology Fund ITS/424/17, ITS/060/18 and the CUHK-SJTU Joint Research Collaboration Fund. *(Corresponding author: Zheng Li.)*

W. Li is with the Chow Yuk Ho Technology Centre for Innovative Medicine, The Chinese University of Hong Kong, Hong Kong, China (e-mail: weibingli@cuhk.edu.hk).

C. Song and Z. Li are with the Department of Surgery and the Chow Yuk Ho Technology Centre for Innovative Medicine, The Chinese University of Hong Kong, Hong Kong, China (e-mail: songchengzhi-inhk@gmail.com; lizheng@cuhk.edu.hk).

joint-displacement and joint-velocity constraints have not been well considered. Unfortunately, joint limits generally exist in a physical robot. Violating joint limits during a task execution process may lead to task failure and even damage the robot. Quadratic programming (QP) based control frameworks have been demonstrated to be powerful alternatives for controlling physically-constrained robots [12]–[15]. Due to the parallel-processing nature and physical implementability, recurrent neural networks (RNNs) have been proposed and implemented as powerful QP solvers [12]–[20]. For instance, in [12], [13], dual neural networks, primal-dual neural networks and numerical algorithms were developed and compared for repetitive motion planning and obstacle avoidance of redundant robots under joint constraints. Following a unifiable procedure, RNNs were designed for kinematic control and manipulability maximization of physically-constrained redundant robots in [14]–[16]. An RNN model was demonstrated to be capable of improving control precision and motion adaptiveness of a surgical robot in [17]. Although joint limits were well handled, visual servoing techniques have not applied to the robots to achieve autonomy in these works. In [18], an RNN model was proposed for visual servoing of an industrial robot with joint limits involved. The above neural networks possess global convergence, which may require infinitely long time to be convergent. For some applications, a faster convergence speed such as finite-time convergence is more preferable. In [19], [20], zeroing neural networks (ZNNs) with accelerated convergence (e.g., finite-time convergence) were applied to kinematic control of redundant robots. However, ZNNs require derivative information of relevant coefficients and it tends to be more complicated and tricky to handle joint limits using ZNNs. Dual neural networks with finite-time convergence were studied in [21], [22], where complex operations such as matrix inversion were involved in the neural networks. Apart from RNNs, other machine learning techniques including feed-forward neural networks and deep reinforcement learning have been developed for redundant robots [23]–[25]. These model-free strategies require a training process and could be promising methods for achieving intelligence, whereas most of the RNN solvers for quadratic programming are model-based and training-free. This work seeks a model-based, inverse-free and training-free RNN solution to ensure finite-time convergence and joint-limit avoidance.

In this paper, kinematics analysis and a QP based control scheme are first presented to achieve visual servoing of a physically-constrained flexible endoscope coupled with a PSM of the dVRK platform. An inverse-free RNN model working as a QP solver is then designed and accelerated to deliver finite-time convergence by using a sign-bi-power activation function (SBPAF). Based on the Lyapunov theory, the finite-time convergence of the accelerated RNN model is mathematically proved, showing that the enhanced RNN model outperforms its predecessor in terms of the convergence speed. To verify the effectiveness of the RNN and the established control framework, computer simulations are performed using a simulated robotic flexible endoscope constructed in the Gazebo simulator and the robot operating system (ROS). The experimentation of the visual servo control framework is finally implemented on a physical robotic flexible endoscope to validate the feasibility of the RNN and the control framework. Simulation and experimental results show that the finite-time convergent RNN model is competent to achieve visual servoing of the robotic flexible endoscope under joint constraints.

The remainder of this paper is organized as follows. In Section II, the robotic flexible endoscope and the kinematics analysis results are introduced. Section III details and analyzes a QP based control scheme and an accelerated RNN for visual servoing of the robotic endoscope. In Sections IV and V, computer simulations and physical experiment are conducted to substantiate the effectiveness of the RNN model and the control scheme. Conclusive remarks are given in Section VI. The main contributions of this paper are listed as follows.

1) The SBPAF is employed to enable an inverse-free RNN to be finite-time convergent. This is the first time to accelerate the RNN model in the literature.
2) Theoretical analysis is conducted with the superiority and finite-time convergence of the accelerated RNN model rigorously proved.
3) Simulation and experimentation of the RNN model are investigated with attractive results substantiating that the proposed control framework is capable of achieving visual servoing of the robotic flexible endoscope with joint limits handled.

Notation: In this paper, symbols $\mathbb{R}^n$ and $\mathbb{R}^{m\times n}$ represent the spaces of n dimensional vectors and $m\times n$ dimensional matrices, respectively. Symbol $^{\mathrm{T}}$ denotes the transpose operator of a vector or matrix. Symbol $\|\cdot\|_r$ stands for the r-norm of a vector. Symbols $\lambda_{\min}(\cdot)$ and $\lambda_{\max}(\cdot)$ indicate the smallest and largest eigenvalues of a matrix, respectively. Symbol $\circ$ denotes the Hadamard product for element-wise multiplication of vectors or matrices.

II. Kinematic Modeling of the Endoscope Robot

The robotic flexible endoscope shown in Fig. 1 possesses six DOFs. Four of the six DOFs are offered by the dVRK robot, while the rest of the two DOFs are provided by the continuum flexible arm. The kinematic modeling of the robotic flexible endoscope involves three kinematic mappings.

A. Mapping of Task and Configuration Spaces

Based on the attached coordinate frames shown in Fig. 1(b), it is easy to determine the first five transformation matrices ${}^{i-1}\boldsymbol{H}_i \in \mathbb{R}^{4\times4}$ with $i=1,2,\cdots,5$. According to [4], [5], the transformation matrix related to the flexible joint is

$$ {}^{5}\boldsymbol{H}_6 = \begin{bmatrix} s_\phi^2 + c_\phi^2 c_\theta & c_\phi s_\phi (c_\theta - 1) & c_\phi s_\theta & \frac{L c_\phi (1-c_\theta)}{\theta} \\ c_\phi s_\phi (c_\theta - 1) & c_\phi^2 + c_\theta s_\phi^2 & s_\phi S_\theta & \frac{L s_\phi (1-c_\theta)}{\theta} \\ -c_\phi s_\theta & -s_\phi s_\theta & c_\theta & \frac{L s_\theta}{\theta} \\ 0 & 0 & 0 & 1 \end{bmatrix}, $$

where $s_\phi := \sin(\phi)$, $c_\phi := \cos(\phi)$, $s_\theta := \sin(\theta)$, $c_\theta := \cos(\theta)$, and parameters ϕ, θ and L represent the bending direction, bending angle and length of the flexible joint, respectively. The final transformation matrix between the end point of the flexible segment and the camera is ${}^{6}\boldsymbol{H}_7$. In light of the

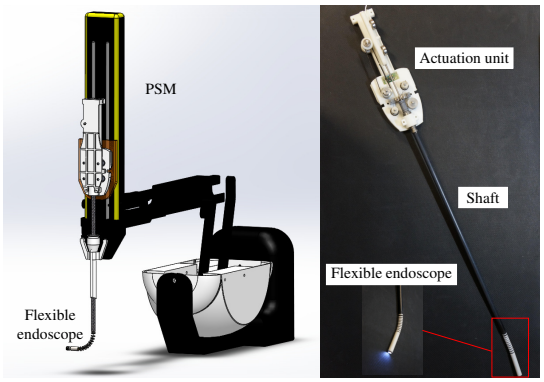

(a)

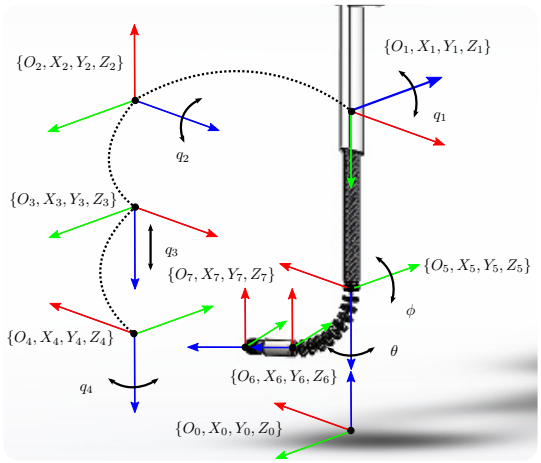

(b)

Fig. 1. A robotic flexible endoscope coupled with a PSM of the dVRK platform. (a) Robotic flexible endoscope. (b) Coordinate frames.

resultant transformation matrices, it is readily to link the pose of the camera and the joint variables:

$$\begin{bmatrix} {}^0\boldsymbol{R}_7 & {}^0\boldsymbol{p}_7 \\ \boldsymbol{0} & 1 \end{bmatrix} = \prod_{i=1}^{7} {}^{i-1}\boldsymbol{H}_i \in \mathbb{R}^{4\times 4} \tag{1}$$

and naturally the velocity-level kinematic equation is

$${}^0\dot{\boldsymbol{\chi}} = \boldsymbol{J}_{\mathrm{t}}\dot{\boldsymbol{q}}, \tag{2}$$

where ${}^0\boldsymbol{R}_7 \in \mathbb{R}^{3\times 3}$ and ${}^0\boldsymbol{p}_7 \in \mathbb{R}^3$ are the rotation matrix and position vector of the camera with respect to the world frame; ${}^0\dot{\boldsymbol{\chi}} = [{}^0\boldsymbol{v}_{\mathrm{c}}^{\mathrm{T}}, {}^0\boldsymbol{w}_{\mathrm{c}}^{\mathrm{T}}]^{\mathrm{T}} \in \mathbb{R}^6$ is the linear and angular velocities of the camera in the world frame. Matrix $\boldsymbol{J}_{\mathrm{t}} \in \mathbb{R}^{6\times 6}$ and vector $\dot{\boldsymbol{q}} = [\dot{\vartheta}_1, \dot{\vartheta}_2, \dot{\vartheta}_3, \dot{\vartheta}_4, \dot{\phi}, \dot{\theta}]^{\mathrm{T}} \in \mathbb{R}^6$ represent the task Jacobian and the joint-velocity vector, respectively.

B. Mapping of Configuration Space and Image Space

For visual servo control, assume a point $\boldsymbol{P}(x, y, z)$ in the camera frame is projected to a point $\boldsymbol{s} = [u, v]^{\mathrm{T}} \in \mathbb{R}^2$ on the image plane. The velocity of point $\dot{\boldsymbol{s}} = [\dot{u}, \dot{v}]^{\mathrm{T}}$ on the image plane and the instantaneous linear and angular velocities of the camera ${}^7\dot{\boldsymbol{\chi}} = [{}^7\boldsymbol{v}_{\mathrm{c}}^{\mathrm{T}}, {}^7\boldsymbol{w}_{\mathrm{c}}^{\mathrm{T}}]^{\mathrm{T}}$ are connected by the following kinematic equation [26]:

$$\dot{\boldsymbol{s}} = \boldsymbol{J}_{\mathrm{image}}\,{}^7\dot{\boldsymbol{\chi}}, \tag{3}$$

where the image Jacobian matrix $\boldsymbol{J}_{\mathrm{image}} \in \mathbb{R}^{2\times 6}$ is

$$\boldsymbol{J}_{\mathrm{image}} = \begin{bmatrix} -\frac{\bar{f}}{z} & 0 & \frac{\bar{u}}{z} & \frac{\bar{u}\bar{v}}{\bar{f}} & -\frac{\bar{f}^2+\bar{u}^2}{\bar{f}} & \bar{v} \\ 0 & -\frac{\bar{f}}{z} & \frac{\bar{v}}{z} & \frac{\bar{f}^2+\bar{v}^2}{\bar{f}} & -\frac{\bar{u}\bar{v}}{\bar{f}} & -\bar{u} \end{bmatrix} \tag{4}$$

with $\bar{u} = u - u_0$, $\bar{v} = v - v_0$ and $\bar{f} = f/\rho$. Here, $\boldsymbol{s}_0 = [u_0, v_0]^{\mathrm{T}}$ is the principal point on the image plane, f and ρ are the focal length of the camera and the pixel width of each square pixel of an image. Depth z can be assumed constant due to the inherent error tolerance of visual servoing [26].

Note that ${}^7\dot{\boldsymbol{\chi}}$ and ${}^0\dot{\boldsymbol{\chi}}$ are depicted in terms of different coordinate frames. Combining kinematic equations (2) and (3), a final kinematic equation is obtained as

$$\dot{\boldsymbol{s}} = \bar{\boldsymbol{J}}\dot{\boldsymbol{q}}, \tag{5}$$

where $\bar{\boldsymbol{J}} := \boldsymbol{J}_{\mathrm{image}}\boldsymbol{J}_{\mathrm{camera}} \in \mathbb{R}^{2\times 6}$ with the camera Jacobian

$$\boldsymbol{J}_{\mathrm{camera}} = \begin{bmatrix} {}^0\boldsymbol{R}_7 & \boldsymbol{0} \\ \boldsymbol{0} & {}^0\boldsymbol{R}_7 \end{bmatrix}^{\mathrm{T}} \boldsymbol{J}_{\mathrm{t}} \in \mathbb{R}^{6\times 6}. \tag{6}$$

C. Mapping of Configuration and Actuation Spaces

The two DOFs associated with the bending direction and bending angle of the flexible joint are driven by four cables. According to [4], [5], [9], the velocity-level kinematic equation is compactly written as

$$\begin{bmatrix} \dot{l}_1 \\ \dot{l}_2 \end{bmatrix} = r_1 \boldsymbol{J}_{\mathrm{actuator}} \begin{bmatrix} \dot{\phi} \\ \dot{\theta} \end{bmatrix} \text{ with } \boldsymbol{J}_{\mathrm{actuator}} = \begin{bmatrix} \theta s_\phi & -c_\phi \\ -\theta c_\phi & -s_\phi \end{bmatrix}, \tag{7}$$

where r_1 is the radius of the circularly distributed chambers and $\dot{l}_i$ denotes the velocity of the ith cable with $\dot{l}_1 + \dot{l}_3 = 0$ and $\dot{l}_2 + \dot{l}_4 = 0$ satisfied. Considering that the cables are operated by two pulley wheels, it further yields

$$\begin{bmatrix} \dot{\vartheta}_5 \\ \dot{\vartheta}_6 \end{bmatrix} = \frac{r_1}{r_2} \boldsymbol{J}_{\mathrm{actuator}} \begin{bmatrix} \dot{\phi} \\ \dot{\theta} \end{bmatrix}, \tag{8}$$

where $\dot{\vartheta}_5$, $\dot{\vartheta}_6$ and r_2 denote the rotary velocities and the radius of the two pulley wheels with $\dot{l}_1 = r_2\dot{\vartheta}_5$ and $\dot{l}_2 = r_2\dot{\vartheta}_6$. Kinematic equations (5) and (8) indicate that variables depicting the motions of the flexible joint can be $\dot{\phi}$ and $\dot{\theta}$ or $\dot{\vartheta}_5$ and $\dot{\vartheta}_6$. Computing $\dot{\phi}$ and $\dot{\theta}$ from $\dot{\vartheta}_5$ and $\dot{\vartheta}_6$ requires the inverse of matrix $\boldsymbol{J}_{\mathrm{actuator}} \in \mathbb{R}^{2\times 2}$. Since matrix $\boldsymbol{J}_{\mathrm{actuator}}$ is singular when $\theta = 0$ rad, $\dot{\phi}$ and $\dot{\theta}$ are chosen as the flexible joint's variables in this paper. In this way, kinematic equation (8) allows one to determine $\dot{\vartheta}_5$, $\dot{\vartheta}_6$ from the resolved variables $\dot{\phi}$ and $\dot{\theta}$ for actuating the physical flexible endoscope.

III. Visual Servo Controller of the Robotic Flexible Endoscope

This section details the mathematical derivations of a QP based visual servo control scheme and a finite-time convergent RNN controller. Then, the finite-time convergence of the RNN controller is theoretically analyzed.

A. Scheme Formulation and RNN Controller

When controlling the dVRK based flexible endoscope, kinematic constraints depicted in (5) must be satisfied. Meanwhile, the resolved joint variables should be bounded by their joint limits. To let the PSM occupy less space when performing a task, the motions of the PSM can be constrained while the movements of the flexible joint can be increased [5]. The following QP based minimum weighted velocity norm (MWVN) scheme meets the above discussed requirements:

$$\text{minimize: } \dot{\boldsymbol{q}}^{\mathrm{T}}\boldsymbol{A}\dot{\boldsymbol{q}}/2, \tag{9}$$

$$\text{subject to: } \bar{\boldsymbol{J}}\dot{\boldsymbol{q}} = \dot{\boldsymbol{s}}, \tag{10}$$

$$\boldsymbol{q}^{-} \leqslant \boldsymbol{q} \leqslant \boldsymbol{q}^{+}, \tag{11}$$

$$\dot{\boldsymbol{q}}^{-} \leqslant \dot{\boldsymbol{q}} \leqslant \dot{\boldsymbol{q}}^{+}, \tag{12}$$

where matrix $\boldsymbol{A} = \boldsymbol{W}^{\mathrm{T}}\boldsymbol{W} = \mathrm{diag}(w_1^2, w_2^2, \cdots, w_6^2) \in \mathbb{R}^{6\times 6}$ with $\boldsymbol{W} := \mathrm{diag}(w_1, w_2, \cdots, w_6)$ and $w_i > 0$ for $i = 1, 2, \cdots, 6$ are used to achieve weighted motions of the robotic endoscope. In addition, $\boldsymbol{q}^{-} \in \mathbb{R}^6$ and $\boldsymbol{q}^{+} \in \mathbb{R}^6$ ($\dot{\boldsymbol{q}}^{-} \in \mathbb{R}^6$ and $\dot{\boldsymbol{q}}^{+} \in \mathbb{R}^6$) respectively denote the lower and upper limits of joint-displacement vector $\boldsymbol{q}$ (joint-velocity vector $\dot{\boldsymbol{q}}$). MWVN scheme (9)–(12) reduces to the minimum velocity norm (MVN) scheme when $\boldsymbol{A} = \boldsymbol{I}$ is an identity matrix.

Equivalently, QP problem (9)–(12) can be formulated as

$$\text{minimize: } \dot{\boldsymbol{x}}^{\mathrm{T}}\dot{\boldsymbol{x}}/2, \tag{13}$$

$$\text{subject to: } \hat{\boldsymbol{J}}\dot{\boldsymbol{x}} = \dot{\boldsymbol{s}}, \tag{14}$$

$$\boldsymbol{x}^{-} \leqslant \boldsymbol{x} \leqslant \boldsymbol{x}^{+}, \tag{15}$$

$$\dot{\boldsymbol{x}}^{-} \leqslant \dot{\boldsymbol{x}} \leqslant \dot{\boldsymbol{x}}^{+}, \tag{16}$$

where $\boldsymbol{x} := \boldsymbol{W}\boldsymbol{q} \in \mathbb{R}^6$, $\dot{\boldsymbol{x}} := \boldsymbol{W}\dot{\boldsymbol{q}} \in \mathbb{R}^6$, $\hat{\boldsymbol{J}} := \bar{\boldsymbol{J}}\boldsymbol{M} \in \mathbb{R}^{2\times 6}$ with $\boldsymbol{M} := \boldsymbol{W}^{-1} = \mathrm{diag}(1/w_1, 1/w_2, \cdots, 1/w_6) \in \mathbb{R}^{6\times 6}$, $\boldsymbol{x}^{-} := \boldsymbol{W}\boldsymbol{q}^{-} \in \mathbb{R}^6$, $\boldsymbol{x}^{+} := \boldsymbol{W}\boldsymbol{q}^{+} \in \mathbb{R}^6$, $\dot{\boldsymbol{x}}^{-} := \boldsymbol{W}\dot{\boldsymbol{q}}^{-} \in \mathbb{R}^6$ and $\dot{\boldsymbol{x}}^{+} := \boldsymbol{W}\dot{\boldsymbol{q}}^{+} \in \mathbb{R}^6$.

The bound constraints (15) and (16) can be unified as a single bound constraint: $\boldsymbol{\xi}^{-} \leqslant \dot{\boldsymbol{x}} \leqslant \boldsymbol{\xi}^{+}$ with

$$\begin{cases} \boldsymbol{\xi}^{-} := \max\{\eta(\boldsymbol{x}^{-} - \boldsymbol{x}), \dot{\boldsymbol{x}}^{-}\}, \\ \boldsymbol{\xi}^{+} := \min\{\eta(\boldsymbol{x}^{+} - \boldsymbol{x}), \dot{\boldsymbol{x}}^{+}\}, \end{cases} \tag{17}$$

where parameter $\eta > 0$ is a constant [12], [13]. Then, QP problem (13)–(16) is consequently rewritten as

$$\text{minimize: } \dot{\boldsymbol{x}}^{\mathrm{T}}\dot{\boldsymbol{x}}/2, \tag{18}$$

$$\text{subject to: } \hat{\boldsymbol{J}}\dot{\boldsymbol{x}} = \dot{\boldsymbol{s}}, \tag{19}$$

$$\boldsymbol{\xi}^{-} \leqslant \dot{\boldsymbol{x}} \leqslant \boldsymbol{\xi}^{+}. \tag{20}$$

According to the KKT conditions of QP (18)–(20), the following equations hold true [18], [27]:

$$\begin{cases} \dot{\boldsymbol{x}} + \hat{\boldsymbol{J}}^{\mathrm{T}}\boldsymbol{\lambda} + \boldsymbol{\mu} = \boldsymbol{0}, \\ \hat{\boldsymbol{J}}\dot{\boldsymbol{x}} = \dot{\boldsymbol{s}}, \\ \dot{\boldsymbol{x}} = \mathcal{P}(\dot{\boldsymbol{x}} + \boldsymbol{\mu}), \end{cases} \tag{21}$$

where $\boldsymbol{\lambda} \in \mathbb{R}^2$ and $\boldsymbol{\mu} \in \mathbb{R}^6$ are the Lagragian multipliers, and the projector operator

$$\mathcal{P}(z_i) = \begin{cases} \xi_i^{+}, & \text{if } z_i > \xi_i^{+}, \\ z_i, & \text{if } \xi_i^{-} \leqslant z_i \leqslant \xi_i^{+}, \\ \xi_i^{-}, & \text{if } z_i < \xi_i^{-}, \end{cases} \tag{22}$$

is defined for each scalar element z_i of a given vector $\boldsymbol{z} \in \mathbb{R}^n$ with $i = 1, 2, \cdots, n$. It follows from the above KKT conditions that

$$\hat{\boldsymbol{J}}\mathcal{P}(-\hat{\boldsymbol{J}}^{\mathrm{T}}\boldsymbol{\lambda}) = \dot{\boldsymbol{s}}, \tag{23}$$

since $\boldsymbol{\mu} = -\hat{\boldsymbol{J}}^{\mathrm{T}}\boldsymbol{\lambda} - \dot{\boldsymbol{x}}$, $\dot{\boldsymbol{x}} = \mathcal{P}(-\hat{\boldsymbol{J}}^{\mathrm{T}}\boldsymbol{\lambda})$ and $\hat{\boldsymbol{J}}\dot{\boldsymbol{x}} = \dot{\boldsymbol{s}}$.

Naturally, an RNN model is obtained for solving QP problem (18)–(20):

$$\begin{cases} \text{state equation: } \dot{\boldsymbol{\lambda}} = \gamma\big(\hat{\boldsymbol{J}}\mathcal{P}(-\hat{\boldsymbol{J}}^{\mathrm{T}}\boldsymbol{\lambda}) - \dot{\boldsymbol{s}}\big), & (24) \\ \text{output equation: } \dot{\boldsymbol{x}} = \mathcal{P}(-\hat{\boldsymbol{J}}^{\mathrm{T}}\boldsymbol{\lambda}), & (25) \end{cases}$$

where parameter $\gamma > 0$ is a scaling factor relevant to the convergence performance. RNN model (24) is exactly the originally proposed QP solver presented in [27], where the global convergence of the neural network has been investigated. As proved in [27], the output of the RNN converges to the optimal solution of the QP problem (18)–(20) as time $t \to +\infty$.

Note that RNN model (24) was proposed for MVN scheme. For controlling the robotic endoscope using the MWVN scheme, the following modified and generalized RNN model is proposed as one of the contributions in this paper:

$$\begin{cases} \text{state equation: } \dot{\boldsymbol{\lambda}} = \gamma\mathcal{F}\big(\hat{\boldsymbol{J}}\mathcal{P}(-\hat{\boldsymbol{J}}^{\mathrm{T}}\boldsymbol{\lambda}) - \dot{\boldsymbol{s}}\big), & (26) \\ \text{output equation: } \dot{\boldsymbol{q}} = \boldsymbol{M}\mathcal{P}(-\hat{\boldsymbol{J}}^{\mathrm{T}}\boldsymbol{\lambda}), & (27) \end{cases}$$

where $\mathcal{F}(\cdot)$ is a mapping array consisting of activation functions $f(\cdot)$. Evidently, the generalized neural network (26) reduces to the original RNN model (24) if linear activation function (LAF) $f(x) = x$ is used. With the global convergence property, the original RNN model (24) may require infinitely long time to be convergent. This may fail to obtain timely convergence in some practical applications. To accelerate and enable the RNN model to be convergent in finite time, the following SBPAF is applied to the neural network:

$$f(x) = x + |x|^{r}\mathrm{sign}(x) + |x|^{\frac{1}{r}}\mathrm{sign}(x), \tag{28}$$

where parameter $r \in (0, 1)$. Sign function $\mathrm{sign}(x) = x/|x|$ when $x \neq 0$ and $\mathrm{sign}(x) = 0$ when $x = 0$.

B. Convergence Analysis of the RNN Controller

Let us consider the following dynamical system:

$$\dot{\boldsymbol{x}}(t) = f(\boldsymbol{x}(t), t),\ t \in [0, +\infty), \tag{29}$$

where $\boldsymbol{x}(t) \in \mathbb{R}^n$ denotes the system state having an initial state $\boldsymbol{x}(0) = \boldsymbol{x}_0$. Besides, $\dot{\boldsymbol{x}}(t)$ is the time derivative of $\boldsymbol{x}(t)$ and the origin $\boldsymbol{x}(t) = \boldsymbol{0}$ is supposed as an equilibrium point of system (29).

Definition 1 ([28]): The origin of system (29) is globally asymptotically stable, if every trajectory of system state $\boldsymbol{x}(t, \boldsymbol{x}_0) \to 0$ when time $t \to +\infty$.

Definition 2 ([29]): The origin of system (29) is globally finite-time stable if it is globally asymptotically stable and there exists a locally bounded settling-time function $T : \mathbb{R}^n \to \mathbb{R}_{+} \cup \{0\}$, such that $\boldsymbol{x}(t, \boldsymbol{x}_0) = 0$ for all $t \geqslant T(\boldsymbol{x}_0)$.

Definition 3 ([30]): Given a column vector $\boldsymbol{x} = [x_1, x_2, \cdots, x_n]^{\mathrm{T}} \in \mathbb{R}^n$ and a positive parameter $r \in \mathbb{R}_+$. The r-norm of vector $\boldsymbol{x}$ is defined as $\|\boldsymbol{x}\|_r := (\sum_{i=1}^n |x_i|^r|)^{\frac{1}{r}}$.

Lemma 1 ([30]): Given a column vector $\boldsymbol{x} = [x_1, x_2, \cdots, x_n]^{\mathrm{T}} \in \mathbb{R}^n$ and two positive parameters $a \in \mathbb{R}_+$ and $b \in \mathbb{R}_+$. If $b \leqslant a$, then $\|\boldsymbol{x}\|_a \leqslant \|\boldsymbol{x}\|_b$ holds true.

Based on the above preliminaries, the faster convergence of the SBPAF activated RNN model (26) is first proved in comparison with the original RNN model (24). Then, the finite-time convergence property of the SBPAF activated RNN model (26) is theoretically analyzed.

Theorem 1: Given a QP problem (18)–(20), if SBPAF (28) is employed to activate RNN model (26), then neural state $\boldsymbol{\lambda}$ of RNN model (26), converges to an equilibrium point $\boldsymbol{\lambda}^*$ faster as compared with RNN model (24).

Proof: Let us introduce a vector $\boldsymbol{y} := \hat{\boldsymbol{J}}\mathcal{P}(-\hat{\boldsymbol{J}}^{\mathrm{T}}\boldsymbol{\lambda}) - \dot{\boldsymbol{s}} \in \mathbb{R}^2$ and define a Lyapunov candidate function for RNN model (26) as

$$\mathcal{V} = \frac{1}{2}\|\boldsymbol{y}\|_2^2. \tag{30}$$

By taking the time derivative, it yields

$$\begin{aligned} D^+\mathcal{V} &= \boldsymbol{y}^{\mathrm{T}}\dot{\boldsymbol{y}} = -\boldsymbol{y}^{\mathrm{T}}\hat{\boldsymbol{J}}D^+\big(\mathcal{P}(-\hat{\boldsymbol{J}}^{\mathrm{T}}\boldsymbol{\lambda})\big)\hat{\boldsymbol{J}}^{\mathrm{T}}\dot{\boldsymbol{\lambda}} \\ &= -\gamma\boldsymbol{y}^{\mathrm{T}}\hat{\boldsymbol{J}}D^+\big(\mathcal{P}(-\hat{\boldsymbol{J}}^{\mathrm{T}}\boldsymbol{\lambda})\big)\hat{\boldsymbol{J}}^{\mathrm{T}}\mathcal{F}(\boldsymbol{y}) \\ &= -\gamma\boldsymbol{y}^{\mathrm{T}}\boldsymbol{H}\mathcal{F}(\boldsymbol{y}), \end{aligned} \tag{31}$$

where $D^+\mathcal{V}$ is the upper right Dini derivative of Lyapunov candidate function $\mathcal{V}$, matrix $\boldsymbol{H} := \hat{\boldsymbol{J}}D^+\big(\mathcal{P}(-\hat{\boldsymbol{J}}^{\mathrm{T}}\boldsymbol{\lambda})\big)\hat{\boldsymbol{J}}^{\mathrm{T}} \in \mathbb{R}^{2\times 2}$ and matrix $D^+\big(\mathcal{P}(-\hat{\boldsymbol{J}}^{\mathrm{T}}\boldsymbol{\lambda})\big) \in \mathbb{R}^{6\times 6}$ denotes the upper right Dini derivative of $\mathcal{P}(-\hat{\boldsymbol{J}}^{\mathrm{T}}\boldsymbol{\lambda})$. If an auxiliary variable $\boldsymbol{z} = -\hat{\boldsymbol{J}}^{\mathrm{T}}\boldsymbol{\lambda} \in \mathbb{R}^6$ is defined, then $D^+\big(\mathcal{P}(\boldsymbol{z})\big) := \mathrm{diag}\big(D^+\big(\mathcal{P}(z_1)\big), D^+\big(\mathcal{P}(z_2)\big), \cdots, D^+\big(\mathcal{P}(z_6)\big)\big)$ is a diagonal matrix of which the diagonal elements are

$$D^+\big(\mathcal{P}(z_i)\big) = \begin{cases} 1, & \text{if } \xi_i^- \leqslant z_i < \xi_i^+, \\ 0, & \text{if } z_i < \xi_i^- \text{ or } z_i \geqslant \xi_i^+, \end{cases} \tag{32}$$

for $i = 1, 2, \cdots, 6$. When the LAF is used, it yields

$$D^+\mathcal{V} = -\gamma\boldsymbol{y}^{\mathrm{T}}\boldsymbol{H}\boldsymbol{y} = -\gamma\hat{\boldsymbol{y}}^{\mathrm{T}}D^+\big(\mathcal{P}(-\hat{\boldsymbol{J}}^{\mathrm{T}}\boldsymbol{\lambda})\big)\hat{\boldsymbol{y}} \leqslant 0 \tag{33}$$

with $\hat{\boldsymbol{y}} = \hat{\boldsymbol{J}}^{\mathrm{T}}\boldsymbol{y} \in \mathbb{R}^6$, since diagonal matrix $D^+\big(\mathcal{P}(-\hat{\boldsymbol{J}}^{\mathrm{T}}\boldsymbol{\lambda})\big)$ is positive semi-definite. This means that RNN model (24) is globally convergent.

When SBPAF (28) is used, it leads to

$$\begin{aligned} D^+\mathcal{V} &= -\gamma\boldsymbol{y}^{\mathrm{T}}\boldsymbol{H}\mathcal{F}(\boldsymbol{y}) \\ &= -\gamma\boldsymbol{y}^{\mathrm{T}}\boldsymbol{H}\big(\boldsymbol{y} + |\boldsymbol{y}|^r \circ \mathrm{sign}(\boldsymbol{y}) + |\boldsymbol{y}|^{\frac{1}{r}} \circ \mathrm{sign}(\boldsymbol{y})\big) \\ &= -\gamma\tilde{\boldsymbol{y}}^{\mathrm{T}}\big(\boldsymbol{y} + |\boldsymbol{y}|^r \circ \mathrm{sign}(\boldsymbol{y}) + |\boldsymbol{y}|^{\frac{1}{r}} \circ \mathrm{sign}(\boldsymbol{y})\big) \\ &= -\gamma\tilde{\boldsymbol{y}}^{\mathrm{T}}\boldsymbol{y} - \gamma\tilde{\boldsymbol{y}}^{\mathrm{T}}(|\boldsymbol{y}|^r \circ \mathrm{sign}(\boldsymbol{y})) - \gamma\tilde{\boldsymbol{y}}^{\mathrm{T}}(|\boldsymbol{y}|^{\frac{1}{r}} \circ \mathrm{sign}(\boldsymbol{y})) \end{aligned} \tag{34}$$

with $\tilde{\boldsymbol{y}} := \boldsymbol{H}^{\mathrm{T}}\boldsymbol{y}$ and symbol $\circ$ denoting the Hadamard product. It follows (33) that the following inequality holds true:

$$\boldsymbol{y}^{\mathrm{T}}\boldsymbol{H}\boldsymbol{y} = \tilde{\boldsymbol{y}}^{\mathrm{T}}\boldsymbol{y} = \sum_{i=1}^{2}\tilde{y}_i y_i \geqslant 0. \tag{35}$$

Hence, the following two inequalities are readily satisfied:

$$\begin{aligned} \tilde{\boldsymbol{y}}^{\mathrm{T}}(|\boldsymbol{y}|^r \circ \mathrm{sign}(\boldsymbol{y})) &= \sum_{i=1}^{2}\tilde{y}_i|y_i|^r\mathrm{sign}(y_i) = \sum_{i=1}^{2}\tilde{y}_i y_i|y_i|^{r-1} \\ &\geqslant \min_{i\in\{1,2\}}\{|y_i|^{r-1}\}\sum_{i=1}^{2}\tilde{y}_i y_i \geqslant 0, \end{aligned} \tag{36}$$

and similarly,

$$\tilde{\boldsymbol{y}}^{\mathrm{T}}(|\boldsymbol{y}|^{\frac{1}{r}} \circ \mathrm{sign}(\boldsymbol{y})) \geqslant \min_{i\in\{1,2\}}\{|y_i|^{\frac{1}{r}-1}\}\sum_{i=1}^{2}\tilde{y}_i y_i \geqslant 0. \tag{37}$$

This means that the time derivative of Lyapunov candidate function $\mathcal{V}$, i.e., $D^+\mathcal{V}$ shown in (34) exhibits three negative terms, i.e., $-\gamma\boldsymbol{y}^{\mathrm{T}}\boldsymbol{H}\boldsymbol{y} \leqslant 0$, $-\gamma\boldsymbol{y}^{\mathrm{T}}\boldsymbol{H}(|\boldsymbol{y}|^r \circ \mathrm{sign}(\boldsymbol{y})) \leqslant 0$ and $-\gamma\boldsymbol{y}^{\mathrm{T}}\boldsymbol{H}(|\boldsymbol{y}|^{\frac{1}{r}} \circ \mathrm{sign}(\boldsymbol{y})) \leqslant 0$. By contrast, $D^+\mathcal{V}$ shown in (33) delivers only one negative term $-\gamma\boldsymbol{y}^{\mathrm{T}}\boldsymbol{H}\boldsymbol{y} \leqslant 0$ in the LAF case. Since $-\gamma\boldsymbol{y}^{\mathrm{T}}\boldsymbol{H}\big(\boldsymbol{y} + |\boldsymbol{y}|^r \circ \mathrm{sign}(\boldsymbol{y}) + |\boldsymbol{y}|^{\frac{1}{r}} \circ \mathrm{sign}(\boldsymbol{y})\big) \leqslant -\gamma\boldsymbol{y}^{\mathrm{T}}\boldsymbol{H}\boldsymbol{y} \leqslant 0$, $D^+\mathcal{V}$ in the SBPAF case becomes more negative in comparison with the LAF case, meaning that Lyapunov candidate function $\mathcal{V}$ converges to 0 faster in the SBPAF case. Hence, the SBPAF activated RNN model (26) can deliver an accelerated convergence speed as compared with RNN model (24). This completes the proof. ■

Theorem 2: Given a QP problem (18)–(20), if SBPAF (28) is employed to activate RNN model (26), then neural state $\boldsymbol{\lambda}$ of RNN model (26), converges to an equilibrium point $\boldsymbol{\lambda}^*$ in finite time.

Proof: Let us define a vector $\boldsymbol{y} := \hat{\boldsymbol{J}}\mathcal{P}(-\hat{\boldsymbol{J}}^{\mathrm{T}}\boldsymbol{\lambda}) - \dot{\boldsymbol{s}} \in \mathbb{R}^2$. The following Lyapunov candidate function for RNN model (26) is defined:

$$\mathcal{V} = \frac{1}{2}\|\boldsymbol{y}\|_2^2 + \frac{1}{r+1}\|\boldsymbol{y}\|_{r+1}^{r+1} + \frac{r}{r+1}\|\boldsymbol{y}\|_{\frac{r+1}{r}}^{\frac{r+1}{r}}. \tag{38}$$

By taking the time derivative, it is readily to have

$$\begin{aligned} D^+\mathcal{V} &= \boldsymbol{y}^{\mathrm{T}}\dot{\boldsymbol{y}} + \Big(|\boldsymbol{y}|^r \circ \mathrm{sign}(\boldsymbol{y})\Big)^{\mathrm{T}}\dot{\boldsymbol{y}} + \Big(|\boldsymbol{y}|^{\frac{1}{r}} \circ \mathrm{sign}(\boldsymbol{y})\Big)^{\mathrm{T}}\dot{\boldsymbol{y}} \\ &= \Big(\boldsymbol{y} + |\boldsymbol{y}|^r \circ \mathrm{sign}(\boldsymbol{y}) + |\boldsymbol{y}|^{\frac{1}{r}} \circ \mathrm{sign}(\boldsymbol{y})\Big)^{\mathrm{T}}\dot{\boldsymbol{y}} \\ &= -\mathcal{F}^{\mathrm{T}}(\boldsymbol{y})\hat{\boldsymbol{J}}D^+\big(\mathcal{P}(-\hat{\boldsymbol{J}}^{\mathrm{T}}\boldsymbol{\lambda})\big)\hat{\boldsymbol{J}}^{\mathrm{T}}\dot{\boldsymbol{\lambda}} \\ &= -\gamma\mathcal{F}^{\mathrm{T}}(\boldsymbol{y})\boldsymbol{H}\mathcal{F}(\boldsymbol{y}) \leqslant -\gamma\lambda_{\min}(\boldsymbol{H})\mathcal{F}^{\mathrm{T}}(\boldsymbol{y})\mathcal{F}(\boldsymbol{y}) \\ &= -\gamma\lambda_{\min}(\boldsymbol{H})\|\boldsymbol{y} + |\boldsymbol{y}|^r\mathrm{sign}(\boldsymbol{y}) + |\boldsymbol{y}|^{\frac{1}{r}}\mathrm{sign}(\boldsymbol{y})\|_2^2 \\ &\leqslant -\gamma\lambda_{\min}(\boldsymbol{H})\Big(\|\boldsymbol{y}\|_2^2 + \|\boldsymbol{y}\|_{2r}^{2r} + \|\boldsymbol{y}\|_{\frac{2}{r}}^{\frac{2}{r}}\Big), \end{aligned} \tag{39}$$

where $\lambda_{\min}(\boldsymbol{H})$ denotes the smallest eigenvalue of matrix $\boldsymbol{H} := \hat{\boldsymbol{J}}D^+\big(\mathcal{P}(-\hat{\boldsymbol{J}}^{\mathrm{T}}\boldsymbol{\lambda})\big)\hat{\boldsymbol{J}}^{\mathrm{T}} \in \mathbb{R}^{2\times 2}$ and $D^+\big(\mathcal{P}(-\hat{\boldsymbol{J}}^{\mathrm{T}}\boldsymbol{\lambda})\big) \in \mathbb{R}^{6\times 6}$ is the Dini derivative of $\mathcal{P}(-\hat{\boldsymbol{J}}^{\mathrm{T}}\boldsymbol{\lambda})$, which is the same as that defined in Theorem 1.

By noting that $2r/(r+1) \in (0, 1)$, It follows (38) that

$$\begin{aligned} \mathcal{V}^{\frac{2r}{r+1}} &= \Big(\frac{1}{2}\|\boldsymbol{y}\|_2^2 + \frac{1}{r+1}\|\boldsymbol{y}\|_{r+1}^{r+1} + \frac{r}{r+1}\|\boldsymbol{y}\|_{\frac{r+1}{r}}^{\frac{r+1}{r}}\Big)^{\frac{2r}{r+1}} \\ &\leqslant \Big(\frac{1}{2}\Big)^{\frac{2r}{r+1}}\|\boldsymbol{y}\|_2^{2\times\frac{2r}{r+1}} + \Big(\frac{1}{r+1}\Big)^{\frac{2r}{r+1}}\|\boldsymbol{y}\|_{r+1}^{2r} \\ &\quad + \Big(\frac{r}{r+1}\Big)^{\frac{2r}{r+1}}\|\boldsymbol{y}\|_{\frac{r+1}{r}}^2. \end{aligned} \tag{40}$$

According to Definition 3 and Lemma 1, $\|\boldsymbol{y}\|_{r+1}^{2r} \leqslant \|\boldsymbol{y}\|_{2r}^{2r}$ and $\|\boldsymbol{y}\|_{\frac{r+1}{r}}^{2} \leqslant \|\boldsymbol{y}\|_2^2$ hold true since $2r < r+1$. Meanwhile,

$$\|\boldsymbol{y}\|_2^{2\times\frac{2r}{r+1}} \leqslant \begin{cases} \|\boldsymbol{y}\|_2^{2r} \leqslant \|\boldsymbol{y}\|_{2r}^{2r}, & \text{if } \|\boldsymbol{y}\|_2^2 \leqslant 1, \\ \|\boldsymbol{y}\|_2^2, & \text{if } \|\boldsymbol{y}\|_2^2 > 1, \end{cases} \tag{41}$$

in view of $r < 2r/(r+1) < 1$. Hence, $\|\boldsymbol{y}\|_2^{2\times\frac{2r}{r+1}} \leqslant \|\boldsymbol{y}\|_{2r}^{2r} + \|\boldsymbol{y}\|_2^2$ and thus

$$\begin{aligned} \mathcal{V}^{\frac{2r}{r+1}} \leqslant & \Big(\Big(\frac{1}{2}\Big)^{\frac{2r}{r+1}} + \Big(\frac{r}{r+1}\Big)^{\frac{2r}{r+1}}\Big)\|\boldsymbol{y}\|_2^2 \\ & + \Big(\Big(\frac{1}{2}\Big)^{\frac{2r}{r+1}} + \Big(\frac{1}{r+1}\Big)^{\frac{2r}{r+1}}\Big)\|\boldsymbol{y}\|_{2r}^{2r}. \end{aligned} \tag{42}$$

Taking into account (38) again yields

$$\begin{aligned} \|\boldsymbol{y}\|_{r+1}^{r+1} &= |y_1|^{r+1} + |y_2|^{r+1} = |y_1|^r|y_1| + |y_2|^r|y_2| \\ &\leqslant \frac{1}{2}\sum_{i=1}^{2}(|y_i|^{2r} + |y_i|^2) = \frac{1}{2}(\|\boldsymbol{y}\|_{2r}^{2r} + \|\boldsymbol{y}\|_2^2) \end{aligned} \tag{43}$$

and

$$\|\boldsymbol{y}\|_{\frac{r+1}{r}}^{\frac{r+1}{r}} = |y_1|^{\frac{1}{r}+1} + |y_2|^{\frac{1}{r}+1} \leqslant \frac{1}{2}(\|\boldsymbol{y}\|_{\frac{2}{r}}^{\frac{2}{r}} + \|\boldsymbol{y}\|_2^2). \tag{44}$$

Hence, the following inequality holds true:

$$\mathcal{V} \leqslant \|\boldsymbol{y}\|_2^2 + \frac{1}{2(r+1)}\|\boldsymbol{y}\|_{2r}^{2r} + \frac{r}{2(r+1)}\|\boldsymbol{y}\|_{\frac{2}{r}}^{\frac{2}{r}}. \tag{45}$$

Consequently,

$$\begin{aligned} &\mathcal{V}^{\frac{2r}{r+1}} + \mathcal{V} \leqslant \Big(\Big(\frac{1}{2}\Big)^{\frac{2r}{r+1}} + \Big(\frac{1}{r+1}\Big)^{\frac{2r}{r+1}} + \frac{1}{2(r+1)}\Big)\|\boldsymbol{y}\|_{2r}^{2r} \\ &+ \Big(\Big(\frac{1}{2}\Big)^{\frac{2r}{r+1}} + \Big(\frac{r}{r+1}\Big)^{\frac{2r}{r+1}} + 1\Big)\|\boldsymbol{y}\|_2^2 + \frac{r}{2(r+1)}\|\boldsymbol{y}\|_{\frac{2}{r}}^{\frac{2}{r}} \\ &= \varrho_1\|\boldsymbol{y}\|_{2r}^{2r} + \varrho_2\|\boldsymbol{y}\|_2^2 + \varrho_3\|\boldsymbol{y}\|_{\frac{2}{r}}^{\frac{2}{r}} \\ &\leqslant \varrho_{\max}\Big(\|\boldsymbol{y}\|_2^2 + \|\boldsymbol{y}\|_{2r}^{2r} + \|\boldsymbol{y}\|_{\frac{2}{r}}^{\frac{2}{r}}\Big), \end{aligned} \tag{46}$$

where

$$\varrho_1 := \Big(\frac{1}{2}\Big)^{\frac{2r}{r+1}} + \Big(\frac{1}{r+1}\Big)^{\frac{2r}{r+1}} + \frac{1}{2(r+1)}, \tag{47}$$

$$\varrho_2 := \Big(\frac{1}{2}\Big)^{\frac{2r}{r+1}} + \Big(\frac{r}{r+1}\Big)^{\frac{2r}{r+1}} + 1,\ \varrho_3 := \frac{r}{2(r+1)}, \tag{48}$$

and $\varrho_{\max} := \max\{\varrho_1, \varrho_2, \varrho_3\}$. Then, it follows (39) that

$$D^+\mathcal{V} \leqslant -\frac{\gamma\lambda_{\min}(\boldsymbol{H})}{\varrho_{\max}}\Big(\mathcal{V}^{\frac{2r}{r+1}} + \mathcal{V}\Big). \tag{49}$$

Hence, RNN (26) converges in finite time [21], [22], [31]:

$$t_{\mathrm{c}} = \frac{\varrho_{\max}(r+1)}{\gamma\lambda_{\min}(\boldsymbol{H})(1-r)}\ln\Big(\mathcal{V}_0^{\frac{1-r}{r+1}} + 1\Big), \tag{50}$$

where $\mathcal{V}_0 := \mathcal{V}(0)$ is the initial value of Lyapunov candidate function $\mathcal{V}$. This completes the proof. ■

Theorem 3: Let $\boldsymbol{\lambda}^* \in \mathbb{R}^2$ be an equilibrium point of RNN model (26). Then, the corresponding neural output $\dot{\boldsymbol{q}}^* = \boldsymbol{M}\mathcal{P}(-\hat{\boldsymbol{J}}^{\mathrm{T}}\boldsymbol{\lambda}^*) \in \mathbb{R}^6$ is the optimal solution to the QP based visual servo control problem (9)–(12).

Proof: Since $\boldsymbol{\lambda}^*$ is an equilibrium point of RNN model (26) and $\dot{\boldsymbol{q}}^* = \boldsymbol{M}\mathcal{P}(-\hat{\boldsymbol{J}}^{\mathrm{T}}\boldsymbol{\lambda}^*)$ is the neural output, the following equations hold true:

$$\begin{cases} \hat{\boldsymbol{J}}\mathcal{P}(-\hat{\boldsymbol{J}}^{\mathrm{T}}\boldsymbol{\lambda}^*) = \dot{\boldsymbol{s}}, \\ \dot{\boldsymbol{q}}^* = \boldsymbol{M}\mathcal{P}(-\hat{\boldsymbol{J}}^{\mathrm{T}}\boldsymbol{\lambda}^*). \end{cases} \tag{51}$$

Define two auxiliary vectors $\dot{\boldsymbol{x}}^* := \boldsymbol{W}\dot{\boldsymbol{q}}^* = \mathcal{P}(-\hat{\boldsymbol{J}}^{\mathrm{T}}\boldsymbol{\lambda}^*) \in \mathbb{R}^6$ and $\boldsymbol{\mu}^* := -\hat{\boldsymbol{J}}^{\mathrm{T}}\boldsymbol{\lambda}^* - \mathcal{P}(-\hat{\boldsymbol{J}}^{\mathrm{T}}\boldsymbol{\lambda}^*) \in \mathbb{R}^6$, where matrix $\boldsymbol{W} := \boldsymbol{M}^{-1}$. Then vector $[(\dot{\boldsymbol{x}}^*)^{\mathrm{T}}, (\dot{\boldsymbol{\lambda}}^*)^{\mathrm{T}}, (\dot{\boldsymbol{\mu}}^*)^{\mathrm{T}}]^{\mathrm{T}}$ satisfies the equations shown in (21) which is an equivalent form of the KKT conditions of QP problem (18)–(20). Since the KKT conditions are sufficient and necessary to ensure an optimal solution of QP problem (18)–(20), $\dot{\boldsymbol{x}}^*$ is the optimal solution to QP problem (18)–(20). Due to the equivalence of QP problems depicted in (18)–(20) and (9)–(12), $\dot{\boldsymbol{q}}^* = \boldsymbol{M}\dot{\boldsymbol{x}}^* = \boldsymbol{M}\mathcal{P}(-\hat{\boldsymbol{J}}^{\mathrm{T}}\boldsymbol{\lambda}^*)$ is the optimal solution to the QP based visual servo control problem (9)–(12). This completes the proof. ■

IV. Simulation Validation

To verify the efficacy of the proposed finite-time convergent RNN model (26) for visual servoing of the robotic endoscope, a simulated robotic endoscope is established in Gazebo with the RNN algorithm implemented in ROS. Specifically, a discrete form of RNN solver (26) is constructed. Given a task with a numerical time duration of $t_{\max}$, a sampling gap τ is used to discretize the QP (18)–(20). In each time step $t_k = k\tau$ for $k = 0, 1, \cdots, t_{\max}/\tau$, the kth QP is treated as constant. To solve the kth QP, the neural state $\boldsymbol{\lambda}$ in the kth time step (i.e., $\boldsymbol{\lambda}_k$) is updated using the following algorithm:

$$\boldsymbol{\lambda}_k^i = \boldsymbol{\lambda}_k^{i-1} + h\gamma\mathcal{F}\big(\hat{\boldsymbol{J}}_k\mathcal{P}(-\hat{\boldsymbol{J}}_k^{\mathrm{T}}\boldsymbol{\lambda}_k^{i-1}) - \dot{\boldsymbol{s}}_k\big), \tag{52}$$

which iterates using step size h and iteration number $i = 1, 2, \cdots, i_{\max}$ with $i_{\max} = 5000$ until the solution error $\varepsilon := \|\hat{\boldsymbol{J}}\mathcal{P}(-\hat{\boldsymbol{J}}^{\mathrm{T}}\boldsymbol{\lambda}) - \dot{\boldsymbol{s}}\|_2 < 1\times10^{-3}$ or iteration number i reaches $i_{\max}$. Joint-angle vector $\boldsymbol{q}$ is then updated by considering (27) and Euler's method $\dot{\boldsymbol{q}}_k := (\boldsymbol{q}_{k+1} - \boldsymbol{q}_k)/\tau$:

$$\boldsymbol{q}_{k+1} = \boldsymbol{q}_k + \tau\boldsymbol{M}_k\mathcal{P}(-\hat{\boldsymbol{J}}_k^{\mathrm{T}}\boldsymbol{\lambda}_k). \tag{53}$$

The roles of the weighting matrix $\boldsymbol{A}$ and activation functions are studied with parameters $t_{\max} = \gamma = 5.0$, $h = \tau = 0.01$, $r = 0.5$, $\eta = 6$, $\boldsymbol{q}^- = [-\pi/3\ \text{rad}, -\pi/4\ \text{rad}, 0.08\ \text{m}, -\pi\ \text{rad}, -10^3\pi\ \text{rad}, -\pi/2\ \text{rad}]^{\mathrm{T}}$, $\boldsymbol{q}^+ = [\pi/3\ \text{rad}, \pi/4\ \text{rad}, 0.15\ \text{m}, \pi\ \text{rad}, 10^3\pi\ \text{rad}, \pi/2\ \text{rad}]^{\mathrm{T}}$, $\dot{\boldsymbol{q}}^+ = [2\ \text{rad/s}, 2\ \text{rad/s}, 0.4\ \text{m/s}, 6\ \text{rad/s}, 6\ \text{rad/s}, 6\ \text{rad/s}]^{\mathrm{T}}$, and $\dot{\boldsymbol{q}}^- = -\dot{\boldsymbol{q}}^+$. Simulation results are recorded using ROS bag files. Due to the iterative computations, the recorded ROS time duration would be different from the numerical time duration. The control step time is not strictly fixed and it involves the computing time and the computer-robot interaction time, indicating that the control step time could be larger or smaller than the numerical time step τ.

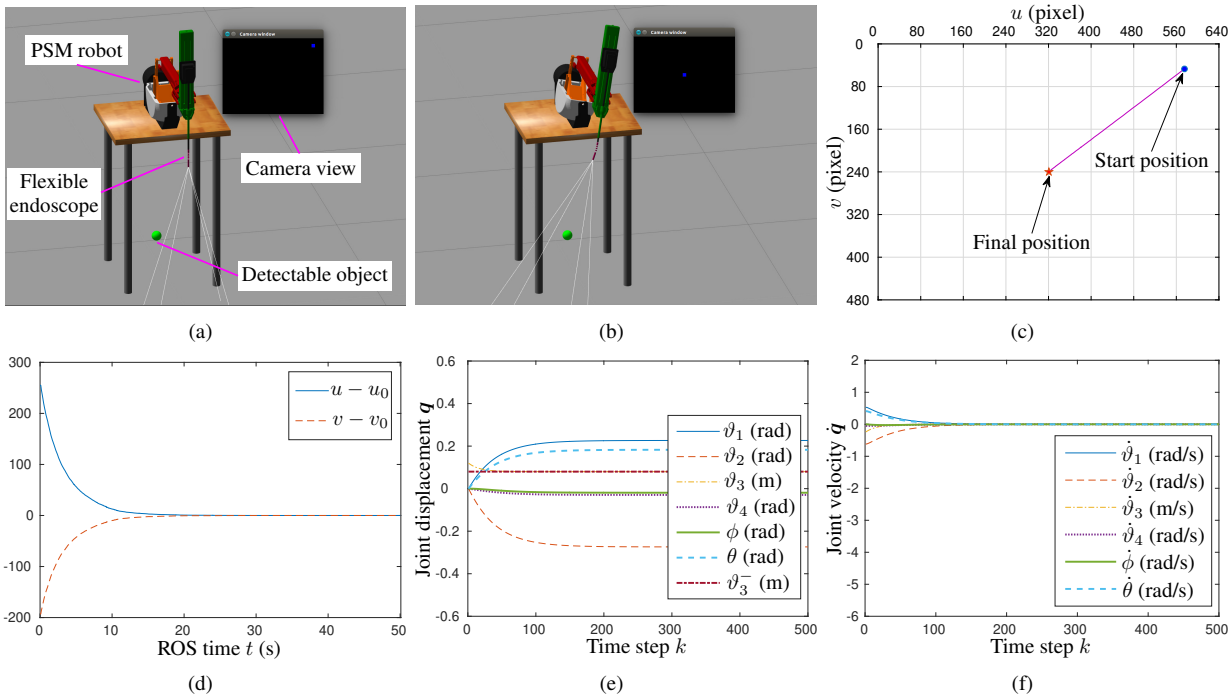

Fig. 2. Visual servo control of the flexible endoscope based on RNN model (26) activated by SBPAF (28) and MVN scheme (9)–(12). (a) Initial state. (b) Final state. (c) Pixel trajectory. (d) Pixel errors. (e) Resolved joint displacements. (f) Resolved joint velocities.

A. Role of Weighting Matrix $\boldsymbol{A}$

Since the performance index in (9) aims to minimize the weighted norm of the joint velocities, weighting matrix $\boldsymbol{A}$ plays a role in constraining or increasing motions of some joints of the robotic flexible endoscope. When $\boldsymbol{A} := \boldsymbol{I}$ is an identity matrix, QP formulation (9)–(12) reduces to an MVN scheme. Simulation results synthesized by the MVN scheme are shown in Fig. 2. As seen from Fig. 2(a)–(d), the flexible endoscope, starting from the initial state shown in Fig. 2(a), finally places the target of interest in the center of the camera view after around 20 s in ROS. The resolved joint displacements and velocities illustrated in Fig. 2(e) and (f) are all bounded by their limits. In particular, joint displacement ϑ_3 reaches but does not exceed its lower limit $\vartheta_3^- = 0.08$ m. This verifies the effectiveness of RNN model (26) for joint limit avoidance. The MVN scheme results in large joint motions of the PSM as can be observed in Fig. 2(b), (e) and (f).

The MWVN scheme (9)–(12) is capable of achieving weighted joint motions of the robotic endoscope. By constraining the movements of the PSM and making the flexible segment more active, the robotic endoscope is enabled to benefit from the dexterity of its flexible joint. To demonstrate this point, weighting matrix $\boldsymbol{A} := \text{diag}\{500, 500, 100, 500, 1, 1\}$ is adopted in MWVN scheme (9)–(12). Corresponding results are shown in Fig. 3. Starting from the same initial state shown in Fig. 2(a), the flexible endoscope bends to track the target. As seen from Fig. 3(a) and (b), the target is successfully placed at the center of the camera view. The resolved joint displacements and velocities illustrated in Fig. 3(c) and (d) show that the motions of the PSM are restricted and the visual task is accomplished by larger motions of the flexible joint as compared with the MVN scheme.

B. Role of Activation Functions

For verifying the superiority of the SBPAF (28), LAF is also applied to activate RNN model (26) to finish the same task. Comparative results are shown in Fig. 3(e) and (f). As shown in these figures, the MVN scheme and the MWVN scheme with LAF used perform more iterations at some time steps during the task execution process, as compared with the MWVN scheme with SBPAF employed. For the first 100 time steps, 0.012 s and 0.006 s are averagely consumed by the LAF and SBPAF cases of the MWVN scheme in each time step, respectively. This leads to a fact that the visual task can be achieved faster by using the SBPAF activated RNN model as presented in Fig. 3(f). After a shorter time of 4 s, the robotic flexible endoscope places the object at the central area of the camera view when MWVN scheme (9)–(12) is utilized. By comparing with the MVN scheme (see Fig. 2), it can conclude that the relatively active role of the flexible joint can be beneficial to speeding up the tracking process and reducing the occupied space of the PSM robot. The superior convergence of the SBPAF activated RNN is thus validated.

C. Comparison with Pseudo-inverse Based Method

One classic pseudo-inverse based solution for robot control is the gradient-projection method [32], [33]:

$$\dot{\boldsymbol{x}} = \hat{\boldsymbol{J}}^{\mathrm{T}}\boldsymbol{Q}\dot{\boldsymbol{s}} + \left(\boldsymbol{I} - \hat{\boldsymbol{J}}^{\mathrm{T}}\boldsymbol{Q}\hat{\boldsymbol{J}}\right)\sum_{i=1}^{n}\kappa_i\nabla\psi_i, \tag{54}$$

where $\boldsymbol{Q} := (\hat{\boldsymbol{J}}\hat{\boldsymbol{J}}^{\mathrm{T}} + \delta^2\boldsymbol{I})^{-1}$ with δ denoting a damping factor; κ_i is a scalar gain; ψ_i is a scalar-valued optimization index

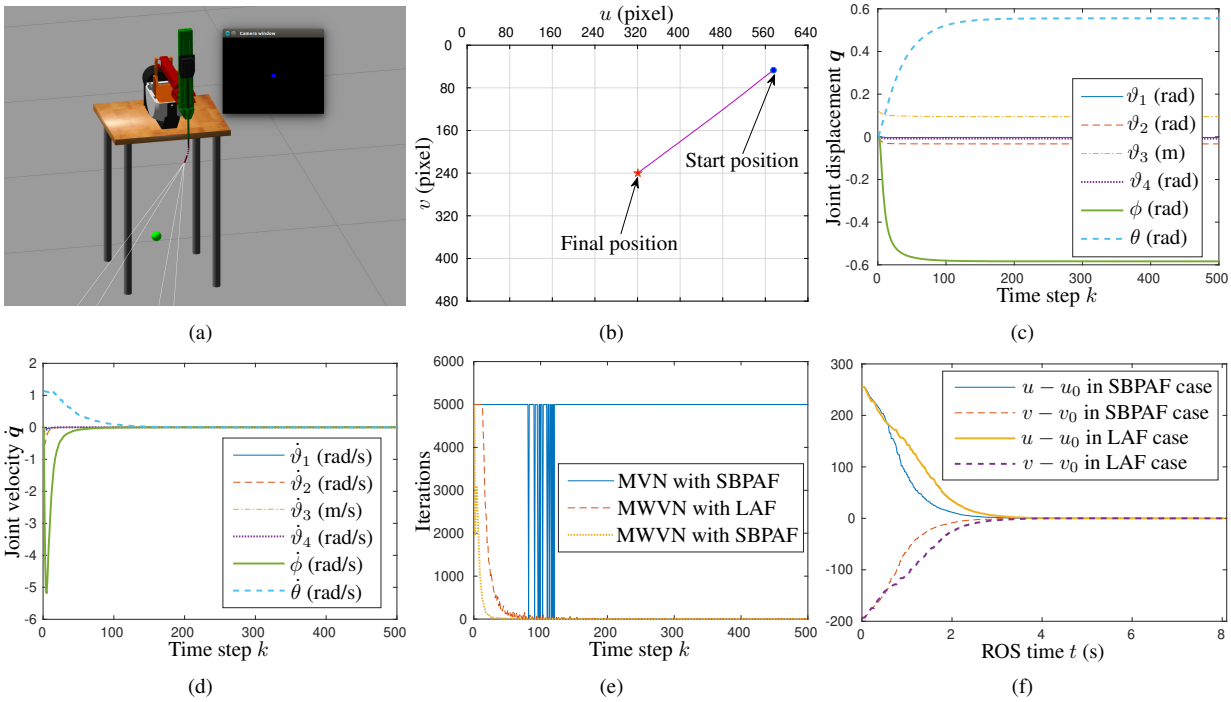

Fig. 3. Visual servo control of the flexible endoscope based on SBPAF (28) and LAF activated RNN model (26) and MVN/MWVN scheme (9)–(12). (a) Final state of the MWVN scheme with SBPAF used. (b) Pixel trajectory of the MWVN scheme with SBPAF used. (c) Resolved joint displacements of the MWVN scheme with SBPAF used. (d) Resolved joint velocities of the MWVN scheme with SBPAF used. (e) Iterations of the MVN and MWVN schemes. (f) Pixel errors of the MWVN scheme with SBPAF and LAF used.

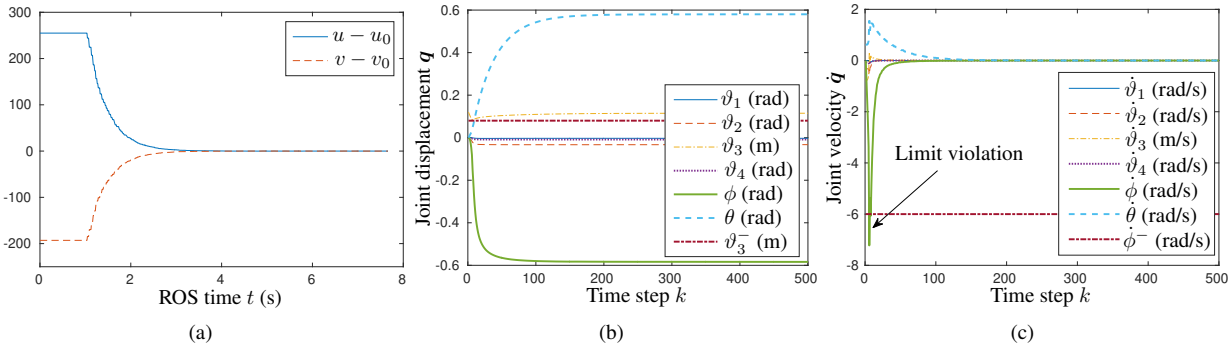

Fig. 4. Visual servo control of the flexible endoscope using pseudo-inverse based scheme (55) with $\boldsymbol{A} := \text{diag}\{500, 500, 100, 500, 1, 1\}$, $\kappa_1 = 1 \times 10^{-3}$ and $\kappa_2 = 1 \times 10^{-5}$. (a) Pixel errors. (b) Resolved joint displacements. (c) Resolved joint velocities.

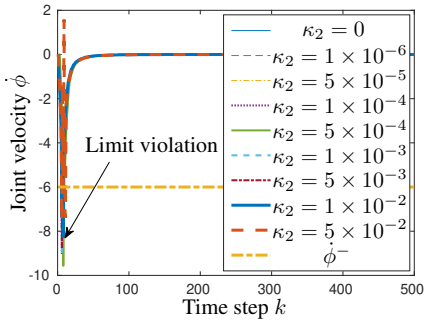

Fig. 5. Resolved joint velocity $\dot{\phi}$ synthesized by visual servoing of the flexible endoscope using pseudo-inverse based scheme (55) with $\boldsymbol{A} := \text{diag}\{500, 500, 100, 500, 1, 1\}$, $\kappa_1 = 1 \times 10^{-3}$ and different values of κ_2.

and ∇ denotes the gradient operator. Considering $\dot{\boldsymbol{x}} := \boldsymbol{W}\dot{\boldsymbol{q}}$ and $\boldsymbol{M} := \boldsymbol{W}^{-1}$, it yields

$$\dot{\boldsymbol{q}} = \boldsymbol{M}\hat{\boldsymbol{J}}^{\mathrm{T}}\boldsymbol{Q}\dot{\boldsymbol{s}} + \boldsymbol{M}\big(\boldsymbol{I} - \hat{\boldsymbol{J}}^{\mathrm{T}}\boldsymbol{Q}\hat{\boldsymbol{J}}\big)\sum_{i=1}^{n}\kappa_i\nabla\psi_i. \tag{55}$$

Control law (55) is the weighted gradient-projection solution presented in [32], [33] by noticing that $\hat{\boldsymbol{J}} := \bar{\boldsymbol{J}}\boldsymbol{M}$. In [33], [34], two performance indices were defined as

$$\psi_1 = \sum_{i=1}^{6}\frac{(q_i^+ - q_i^-)^2}{4(q_i^+ - q_i)(q_i - q_i^-)}, \tag{56}$$

$$\psi_2 = \sum_{i=1}^{6}\frac{(\dot{q}_i^+ - \dot{q}_i^-)^2}{4(\dot{q}_i^+ - \dot{q}_i)(\dot{q}_i - \dot{q}_i^-)}, \tag{57}$$

for avoiding joint-angle and joint-velocity limits, where $\nabla\psi_1 = [\partial\psi_1/\partial q_1, \partial\psi_1/\partial q_2, \cdots, \partial\psi_1/\partial q_6]^{\mathrm{T}}$ and $\nabla\psi_2 = [\partial\psi_2/\partial\dot{q}_1, \partial\psi_2/\partial\dot{q}_2, \cdots, \partial\psi_2/\partial\dot{q}_6]^{\mathrm{T}}$.

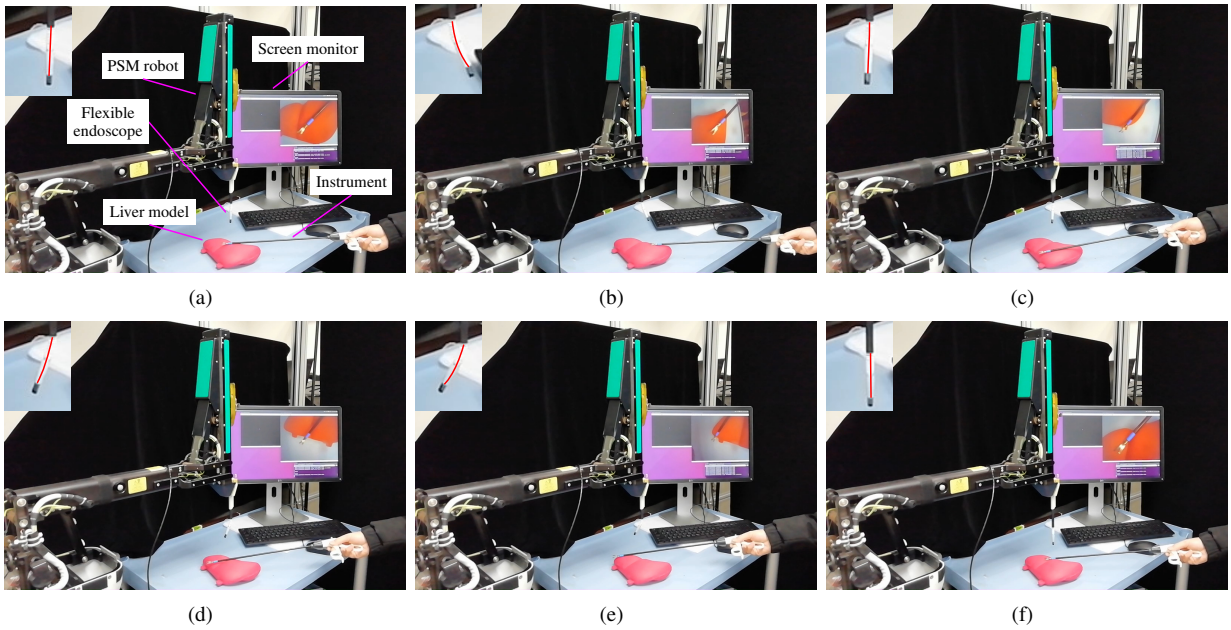

Fig. 6. Visual servo control of the physical flexible endoscope based on SBPAF (28) activated RNN model (26) and MWVN scheme (9)–(12) with $\boldsymbol{A} := \text{diag}\{500, 500, 100, 500, 1, 1\}$ employed. (a) Initial state with labels. (b)–(f) Snapshots during the visual task.

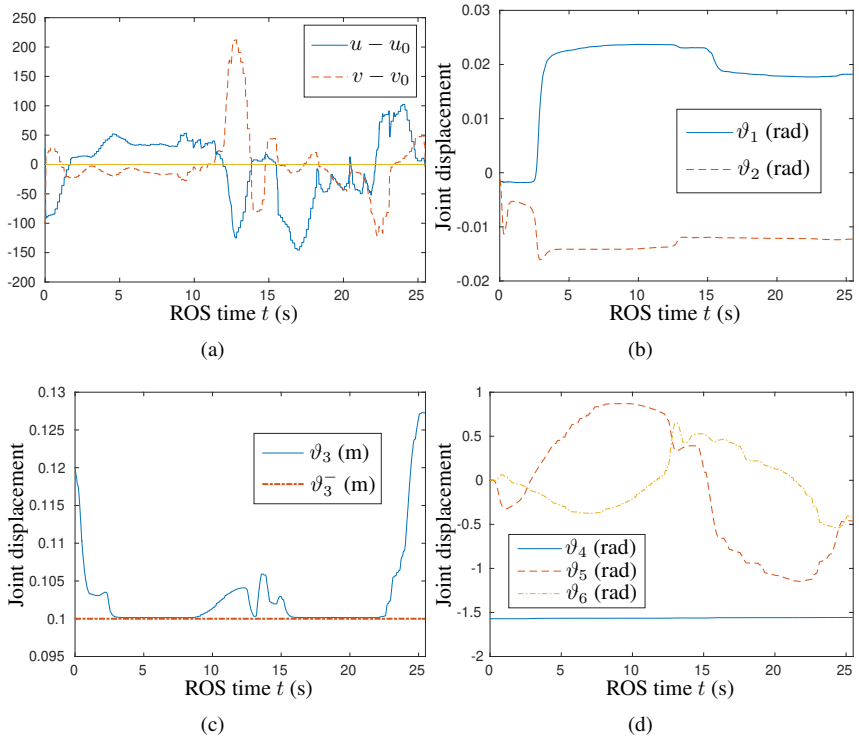

Fig. 7. Experimental results corresponding to the visual servo control of the physical flexible endoscope. (a) Pixel errors. (b) Joint displacements ϑ_1 and ϑ_2. (c) Joint displacement ϑ_3. (d) Joint displacements ϑ_4, ϑ_5 and ϑ_6.

To demonstrate the superiority of the proposed QP based MWVN scheme (9)–(12), the pseudo-inverse based control scheme (55) with performance indices (56) and (57) is applied to visual servoing of the flexible endoscope. The case with weighting matrix $\boldsymbol{A} := \text{diag}\{500, 500, 100, 500, 1, 1\}$ is comparatively investigated. Corresponding results are presented in Figs. 4. The initial state of the robotic flexible endoscope is set as the same as shown in Fig. 2(a). The final state of the robotic endoscope is similar to the one presented in Fig. 3(a) and thus it is omitted due to space limitation. As seen from Fig. 4(a), the pixel errors vanish to be 0, meaning that the detectable object is finally located at the central area of the image plane by adjusting the endoscope automatically using pseudo-inverse based scheme (55). The resolved joint displacements presented in Fig. 4(b) are all within their limits. In particular, joint displacement ϑ_3 approaches its lower limit

ϑ_3^- in the first few time steps. When the joint displacement ϑ_3 is close to its lower limit, performance index (56) takes effect to enable the joint to move away from its lower limit. However, the resolved joint velocity $\dot{\phi}$ shown in Fig. 4(c) violates its lower limit, which is undesirable. Since the parameter κ_2 is claimed to be relevant to joint-velocity avoidance, cases with different values of κ_2 have been studied. Fig. 5 presents the resolved joint velocity $\dot{\phi}$, showing that the joint limit violation phenomenon cannot be eliminated. Note that a too large value of κ_2 (e.g., 0.1) would lead to unstability of the pseudo-inverse based control scheme. As compared with the QP based scheme, the pixels errors shown in Fig. 3(f) and Fig. 4(a) exhibit almost the same convergence time and time duration in ROS. The joint-limit handling techniques of the two schemes are different. In the pseudo-inverse based scheme, the resolved joint displacement cannot coincide with its limits due to the repulsive velocity applied by performance index (56). In contrast, the joint displacement resolved by the QP based scheme can coincide but never exceed its limits. For handling joint limits, the QP based scheme outperforms the pseudo-inverse based scheme.

V. Experimental Validation

To verify the physical feasibility of the MWVN scheme (9)–(12) and RNN model (26) activated by SBPAF (28), the experimentation of the method is conducted on a physical robotic flexible endoscope shown in Fig. 6(a). A surgical instrument is manually operated to move along the boundary of a liver model. Programs for the experiment are written in C++ on a personal computer with Ubuntu and ROS installed. The lower limit of joint displacement ϑ_3 is set as 0.1 m, while other joint limits are set as the same as those in the simulations. Experimental results are presented in Figs. 6 and 7. Fig. 6 shows the snapshots of the robotic flexible endoscope tracking the instrument. As seen from the snapshots, the flexible endoscope bends to follow the instrument, enabling the instrument to be placed at the central area of the camera view. Transient behaviors of the pixel errors are plotted in Fig. 7(a), showing that the errors vanish to be around 0 during the visual tracking task. The joint-displacement data collected from the physical robot are shown in Fig. 7(b)–(d). All the joint displacements are kept within their joint limits. Particularly, joint displacement ϑ_3 reaches but does not violate its lower limit $\vartheta_3^- = 0.1$ m. The motions of the PSM robot (specifically, ϑ_1 and ϑ_2) are constrained as illustrated in Fig. 7(b), whereas the bending motions of the flexible joint (i.e., ϑ_5 and ϑ_6) shown in Fig. 7(d) play much more active role to finish the visual task. These results substantiate the effectiveness of MWVN scheme (9)–(12) and SBPAF (28) activated RNN model (26) for visual servo control of the physically-constrained robotic flexible endoscope.

VI. Conclusion

For visual servoing of a dVRK based flexible endoscope, the associated kinematic model has been established leading to a QP based MWVN control scheme. As a QP solver, an RNN model has been modified and accelerated to solve the QP problem in finite time. Theoretical analysis has been conducted with the superior convergence performance of the accelerated RNN model proved in comparison with its predecessor. Comparative simulations are performed showing that the MWVN scheme outperforms the MVN scheme and a classic pseudo-inverse based solution. The accelerated RNN model is advantageous over its predecessor in terms of the visual tracking speed. The physical feasibility of the MWVN scheme and the accelerated RNN model has been experimentally validated using a physical flexible endoscope. Both simulation and experimental results have demonstrated that the proposed method can achieve visual servo control of the robotic flexible endoscope and consider the joint limits simultaneously. Future work will focus on monocular and binocular endoscopes that offer depth information by deep learning or measurement strategies.

References

[1] P. Gomes, *Medical Robotics: Minimally Invasive Surgery*. Sawston, Cambridge, UK: Woodhead Publishing Limited, 2012.

[2] J. Troccaz, *Medical Robotics*. Hoboken, NJ, USA: John Wiley & Sons, Inc., 2012.

[3] W. Chen, Y. Lu, B. Yang, G. Ma, Z. Wang, and Y. hui Liu, "Automatic field of view control of laparoscopes with soft RCM constraints," *Proc. World Congr. Intell. Control Autom.*, pp. 653–658, 2018.

[4] L. Ott, F. Nageotte, P. Zanne, and M. de Mathelin, "Robotic assistance to flexible endoscopy by physiological-motion tracking," *IEEE Trans. Robot.*, vol. 27, no. 2, pp. 346–359, Apr. 2011.

[5] X. Ma, C. Song, W. Y. P. Chiu, and Z. Li, "Autonomous flexible endoscope for minimally invasive surgery with enhanced safety," *IEEE Robot. Autom. Lett.*, vol. 4, no. 3, pp. 2607–2613, Jul. 2019.

[6] S. D'Attanasio, O. Tonet, G. Megali, M. C. Carrozza, and P. Dario, "A semi-automatic handheld mechatronic endoscope with collision-avoidance capabilities," in *Proc. IEEE Int. Conf. Robot. Autom.*, vol. 2, pp. 1586–1591, 2000.

[7] H.-S. Yoon and B.-J. Yi, "A 4-DOF flexible continuum robot using a spring backbone," in *Proc. Int. Conf. Mech. Autom.*, pp. 1249–1254, 2009.

[8] D.-G. Choi, B.-J. Yi, and W.-K. Kim, "Design of a spring backbone micro endoscope," in *Proc. IEEE/RSJ Int. Conf. Intell. Robot. Syst.*, pp. 1815–1821, 2007.

[9] Z. Li, M. Z. Oo, V. Nalam, V. D. Thang, H. Ren, T. Kofidis, and H. Yu, "Design of a novel flexible endoscope - cardioscope," *ASME J. Mech. Robot.*, vol. 8, no. 5, pp. 051 014–051 014–9, 2016.

[10] B. P. M. Yeung and P. W. Y. Chiu, "Application of robotics in gastrointestinal endoscopy: A review," *World J. Gastr.*, vol. 22, no. 5, pp. 1811–1825, 2016.

[11] Z. Li and P. W.-Y. Chiu, "Robotic endoscopy," *Visceral Med.*, vol. 34, no. 1, pp. 45–51, Feb. 2018.

[12] Y. Zhang and Z. Zhang, *Repetitive Motion Planning and Control of Redundant Robot Manipulators*. Berlin, Heidelberg, Germany: Springer-Verlag, 2013.

[13] D. Guo and Y. Zhang, "Acceleration-level inequality-based MAN scheme for obstacle avoidance of redundant robot manipulators," *IEEE Trans. Ind. Electron.*, vol. 61, no. 12, pp. 6903–6914, Dec. 2014.

[14] Y. Zhang, S. Chen, S. Li, and Z. Zhang, "Adaptive projection neural network for kinematic control of redundant manipulators with unknown physical parameters," *IEEE Trans. Ind. Electron.*, vol. 65, no. 6, pp. 4909–4920, Jun. 2018.

[15] Y. Zhang, S. Li, and X. Zhou, "Recurrent-neural-network-based velocity-level redundancy resolution for manipulators subject to a joint acceleration limit," *IEEE Trans. Ind. Electron.*, vol. 66, no. 5, pp. 3573–3582, May. 2019.

[16] L. Jin, S. Li, H. M. La, and X. Luo, "Manipulability optimization of redundant manipulators using dynamic neural networks," *IEEE Trans. Ind. Electron.*, vol. 64, no. 6, pp. 4710–4720, Jun. 2017.

[17] Y. Li, S. Li, D. Caballero, M. Miyasaka, A. Lewis, and B. Hannaford, "Improving control precision and motion adaptiveness for surgical robot with recurrent neural network," in *Proc. IEEE/RSJ Int. Conf. Intell. Robot. Syst.*, pp. 3538–3543, Sep. 2017.

[18] Y. Zhang and S. Li, "A neural controller for image-based visual servoing of manipulators with physical constraints," *IEEE Trans. Neural Netw. Learn. Syst.*, vol. 29, no. 11, pp. 5419–5429, Nov. 2018.

[19] W. Li, "A recurrent neural network with explicitly definable convergence time for solving time-variant linear matrix equations," *IEEE Trans. Ind. Informat.*, vol. 14, no. 12, pp. 5289–5298, Dec. 2018.

[20] W. Li, Z. Su, and Z. Tan, "A variable-gain finite-time convergent recurrent neural network for time-variant quadratic programming with unknown noises endured," *IEEE Trans. Ind. Informat.*, vol. 15, no. 9, pp. 5330–5340, Sep. 2019.

[21] S. Li, Y. Li, and Z. Wang, "A class of finite-time dual neural networks for solving quadratic programming problems and its k-winners-take-all application," *Neural Netw.*, vol. 39, pp. 27–39, 2013.

[22] J. Feng, S. Qin, F. Shi, and X. Zhao, "A recurrent neural network with finite-time convergence for convex quadratic bilevel programming problems," *Neural Comput. Appl.*, vol. 30, no. 11, pp. 3399–3408, 2018.

[23] A. S. Polydoros, L. Nalpantidis, and V. Krger, "Real-time deep learning of robotic manipulator inverse dynamics," in *Proc. IEEE/RSJ Int. Conf. Int. Robot. Syst.*, pp. 3442–3448, 2015.

[24] S. Gu, E. Holly, T. Lillicrap, and S. Levine, "Deep reinforcement learning for robotic manipulation with asynchronous off-policy updates," in *Proc. IEEE Int. Conf. Robot. Autom.*, pp. 3389–3396, 2017.

[25] D. Quillen, E. Jang, O. Nachum, C. Finn, J. Ibarz, and S. Levine, "Deep reinforcement learning for vision-based robotic grasping: A simulated comparative evaluation of off-policy methods," in *Proc. IEEE Int. Conf. Robot. Autom.*, pp. 6284–6291, 2018.

[26] P. Corke, *Robotics, Vision and Control: Fundamental Algorithms in MATLAB*. Berlin, Heidelberg, Germany: Springer-Verlag, 2011.

[27] S. Li, S. Chen, B. Liu, Y. Li, and Y. Liang, "Decentralized kinematic control of a class of collaborative redundant manipulators via recurrent neural networks," *Neurocomputing*, vol. 91, pp. 1 – 10, 2012.

[28] G. Piersanti, *The Macroeconomic Theory of Exchange Rate Crises*. Oxford, UK: Oxford University Press, 2012.

[29] J. P. LaSalle and S. Lefschetz, *Stability by Liapunov's Direct Method with Applications*. New York, NY, USA: Academic Press, 1961.

[30] G. Golub and C. Van Loan, *Matrix Computations*. Baltimore, MD, USA: Johns Hopkins University Press, 1983.

[31] Y. Shen and Y. Huang, "Uniformly observable and globally Lipschitzian nonlinear systems admit global finite-time observers," *IEEE Trans. Autom. Control*, vol. 54, no. 11, pp. 2621–2625, 2009.

[32] T. Hu, T. Wang, J. Li, and W. Qian, "Gradient projection of weighted Jacobian matrix method for inverse kinematics of a space robot with a controlled-floating base," *J. Dynamic Syst., Measur., Control*, vol. 139, no. 5, 2017, 051013.

[33] J. Wan, J. Yao, L. Zhang, and H. Wu, "A weighted gradient projection method for inverse kinematics of redundant manipulators considering multiple performance criteria," *Stroj. vestn. - J. Mech. Eng.*, vol. 64, no. 7-8, pp. 475–487, 2018.

[34] H. Zghal, R. V. Dubey, and J. A. Euler, "Efficient gradient projection optimization for manipulators with multiple degrees of redundancy," in *Proc. IEEE Int. Conf. Robot. Autom.*, pp. 1006–1011, 1990.

Weibing Li received the B.S. degree in communication engineering from Changchun University, Changchun, China, in 2011, the M.S. degree in detection technology and automatic equipment from Sun Yat-sen University, Guangzhou, China, in 2014, and the Ph.D. degree in mechanical engineering from University of Leeds, Leeds, U.K., in 2018.

He is currently a Post-Doctoral Fellow with the Chow Yuk Ho Technology Centre for Innovative Medicine, The Chinese University of Hong Kong, Hong Kong, China. His current research interests include industrial robotics, modular robotics, medical robotics, and neural networks.

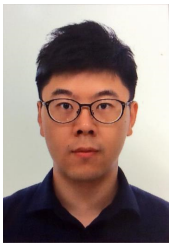

Chengzhi Song received the B.S. degree in automation from Xiamen University, Xiamen China, and the M.S. degree in Electronic Engineering from the Hong Kong University of Science and Technology, Hong Kong, China, in 2013 and 2014, respectively. He is currently working towards the Ph.D. degree in Surgery at the Chinese University of Hong Kong, Hong Kong, China. His research interests include medical robotics, flexible robotics and laparoscopy.

Zheng Li received the B. Eng. and M. Eng. degrees in mechanical and automation engineering from Beihang University, Beijing, China, in 2007 and 2010 respectively, and the Ph.D. degree in robotics from The Chinese University of Hong Kong, Hong Kong, China, in 2013. He is a member of IEEE and ASME.

He is currently an assistant professor at the Department of Surgery and Chow Yuk Ho Technology Centre for Innovative Medicine, The Chinese University of Hong Kong, Hong Kong, China. His research interests include design, kinematic modeling, sensing, and control of flexible and soft robots for medical applications.